International Journal of Solids and Structures 299 (2024) 112891

Contents lists available at ScienceDirect

International Journal of Solids and Structures

journal homepage: www.elsevier.com/locate/ijsolstr

Application of mesh-free and finite element methods in modelling nano-scale material removal from copper substrates: A computational approach

Rahul Yadav [a], Anuj Sharma [d], Sivakumar Kulasegaram [a,*], Sahar Alimohammadi [b], Dan Read [b,c], Emmanuel Brousseau [a]

[a] School of Engineering, Cardiff University, United Kingdom
[b] School of Physics and Astronomy, Cardiff University, United Kingdom
[c] Department of Electrical and Computer Engineering, University of California Santa Barbara, United States
[d] Birla Institute of Technology And Science, Pilani, India

ARTICLE INFO

Keywords:
Nano-scratching
SPH
FEM
Ploughing
Cutting
Deformation

ABSTRACT

This study explores the modelling methodology using mesh-free smoothed particle hydrodynamics (SPH) and finite element modelling (FE) techniques to simulate the AFM-based nano-scratching processes for advancing precision engineering in nanotechnology. Tip wear in nano machining substantially increases the tip radius, thereby influencing the material removal mechanism and subsequently affecting the quality of machined nanostructures. In this context, this study examines the effects of rake angle (the inclination of the main cutting edge to the plane perpendicular to the scratched surface), tip radius and scratching depth on cutting forces, groove dimensions, and deformed thickness. This was achieved by implementing an in-house SPH method based particle code employing a Lagrangian algorithm, and an FE model incorporating the dynamic explicit algorithm implemented (in ABAQUS) to carry out nano-scratching simulations. The investigation revealed that the cutting mechanism transitioned to ploughing when the scratching depth decreased to 30% of the tip radius for OFHC-Cu workpiece material machined with a diamond tip. The dominance of normal forces over cutting forces during scratching indicated the side flow of material in the vicinity of the tip radius under intense contact pressure. The ploughing mechanism exhibited more sensitivity at a higher negative rake angle of 60°. Increased scratching depth and tip radius led to more significant material deformation owing to the induction of higher cutting forces, with the maximum deformation thickness 3.6 times the tip radius. The simulated results demonstrated favourable concordance with the experimental data.

1. Introduction

A rapid emergence of fabrication technologies in past decades has improved the achievable accuracies and tolerances to the nanoscale level for a diverse range of applications such as in the electronic, biomedical, optic and communication sectors. The tip based nano-scratching process has been reported as a cost-effective and reliable technique for the generation of nano-scale grooves, slots, and channels on different substrate materials (Bhushan et al., 1995; Mo et al., 2008). In particular, atomic force microscopy (AFM) based systems can be readily employed to generate nano-scale grooves on diverse substrate materials. When implementing this process, the choice of the AFM tip material is crucial and depends on specific application requirements. Diamond AFM tips are commonly utilised because of their durability and high wear resistance, making them well-suited for different applications (Kawasegi et al., 2006).

The AFM probe tip geometry and the process parameters such as tip radius and cutting depth are influential factors affecting material removal at the nanoscale. Depending on the combination of tip geometry, tip material, process parameters and workpiece material, the tip can be subjected to gradual abrasion wear during continuous scratching operations on the nanoscale as a result of the mechanical interaction between the probe and the sample surface (Kong et al., 2020). Consequently, the tip wear affects the accuracy and reliability of the process as

* Corresponding author.
E-mail address: kulasegarams@cardiff.ac.uk (S. Kulasegaram).

https://doi.org/10.1016/j.ijsolstr.2024.112891
Received 30 January 2024; Received in revised form 13 May 2024; Accepted 20 May 2024
Available online 25 May 2024

the changing tip shape can alter force profiles. In particular, abrasion wear occurring at the tooltip typically leads to alterations in the tip radius, thereby it has the potential to modify the effective rake angle for the material flow and influence both the normal and cutting forces. As a result, such tip wear can alter the scratching mechanisms, for example shifting from cutting towards ploughing, especially when the effective negative rake angle and associated tip radius are excessively high (Zhu et al., 2019). Tip wear progresses gradually during the nano-scratching process due to its slow-speed nature. Nonetheless, after a substantial duration, the consequences of wear can become noticeable on both the tip and the scratched profile.

Post-machining, the processed surface may have been subjected to more severe plastic deformation due to tip wear, which in turn should affect component quality in terms of fatigue life and tribological properties. Due to experimental challenges inherent to nano-scale characterisation and processing, numerical modelling is an complementary and effective approach to study nano-scale material removal. Molecular Dynamics (MD) simulation is a commonly used technique for exploring nano-scale machining processes (Jian-Hao et al., 2021; Chen et al., 2021; Xie et al., 2022). With this computational technique, interactions between individual atoms and molecules are modelled over time, providing insights into the intricate dynamics of material removal, tool interactions, and surface characteristics (Wang et al., 2022). For example, the nanoscale wear characteristics of aluminium matrix composites reinforced with SiC particles were investigated through nano-scratching by Yin and co-workers (Yin et al., 2021). The study revealed evidence of dislocation strengthening that led to work hardening. Using MD simulation, Qi et al., (2021) showed that the higher shear strain was concentrated at the shear plane during nano-scratching of the high entropy alloy CoCrFeMnNi. The machining of single crystal silicon with a larger half-apex angle of the tool was modelled and predicted to lead to high chip volume and enhanced smoothness of the scratched surface due to the induction of higher hydrostatic stress (Dai et al., 2019a). The increase in the simulated cutting tip speed from 10 m/sec to 200 m/sec on a SiC substrate led to a reduction in both principal and hydrostatic stress, attributed to the prevalence of thermal softening over the strain rate hardening of the SiC material (Meng et al., 2019). An MD study from Zhang et al., (2013) revealed that double tip-scratching was found to be more effective and produced high-quality grooves compared to successive single-tip scratching on the material surface. Dai et al., (2019b) observed that with an increased tool tip radius, subsurface deformation became more pronounced, accompanied by a reduction in the volume of chips. The larger tool tip radius led to a significant negative rake angle, consequently diminishing the cutting action while promoting an increase in the ploughing action between the diamond cutting tool and the copper workpiece.

Molecular dynamics simulations have limitations however, including computational intensity, restricted simulation times, and system sizes. Accurate representation of complex material behaviour in the order of nanoscale may require extensive computational resources. Smooth Particle Hydrodynamics (SPH) models offer some advantages over molecular dynamics simulations for nano-scratching due to their ability to efficiently handle large deformations and scale seamlessly to macroscopic systems. The particle-based SPH method was introduced by (Gingold and Monaghan, 1977; Lucy, 1977) to simulate large deformations in solid mechanics problems. In SPH, the workpiece and tool are represented as discrete particles, allowing for accurate simulation of material removal at the nanoscale facilitating advancements in precision manufacturing. Leroch et al., (2016) employed the SPH algorithm to simulate the nano-scale scratching of annealed oxygen-free high conductivity (OFHC) copper using a rigid spherical indenter. Guo et al., (2017) applied theoretical and numerical modelling of nano-scratching using a finite element tool with rigid indenters and demonstrated that the scratching procedure exhibits directional dependence when the tool possesses a regular three-sided pyramid shape.

The research conducted above mainly centred on modelling and simulating the nano-scratching process with a particular emphasis on studying forces and scratching mechanisms. However, there are limited reports on the investigation of the impact of tooltip wear on the scratching process, particularly concerning the transition from cutting to ploughing phenomena. The present investigation concentrates on applying two modelling methodologies, including the mesh-free smoothed particle hydrodynamics (SPH) method and the finite element method (FEM), to simulate the physical phenomena associated with nanoscale material removal. An in-house program was developed to implement the particle-based SPH method. The results obtained through SPH are validated with existing literature data for specific process parameters. Subsequently, the implemented SPH model is compared with the FE method to verify the robustness of developed algorithm and then validated with experimental results in the literature. This study specifically explores the impact of tooltip wear on both the scratching process and the resulting scratched groove. Additionally, the study examines how the tooltip influences groove dimensions, material removal, and the residual plastic strain in the scratched specimen. The organisation of the content is as follows: Section 2 outlines the numerical formulation for nano-scratching and provides the material properties associated with both the tool and the workpiece. In section 3, a detailed discussion of the obtained numerical results is presented, specifically addressing the influence of various parameters on the scratched groove, forces, and plastic strain. Section 4 concludes the presented study with remarks on the outcomes.

2. Methodology

This section outlines the methodology employed for simulating nanoscale scratching using SPH and FEM, including the utilised contact and material models.

2.1. SPH mesh-free formulation

The computational mesh-free method employed relied on the SPH technique that utilises particles to represent a continuous domain. In a Lagrangian-based framework, essential field variables can be tracked at individual SPH particles, which move with the material deformation. SPH comprises a particle approximation, a continuous entity is depicted using clusters of particles, and the property of a particle is represented as a weighted average of values linked to neighbouring particles shown in Fig. 1. These SPH particles interact through the utilisation of a kernel function as expressed in Eq. (1).

$$< f_h(\boldsymbol{x}) >= \int f(\boldsymbol{x}_i) W(|\boldsymbol{x}_i - \boldsymbol{x}_j|, h) d\Omega \tag{1}$$

In this context, $< f_h(\boldsymbol{x}) >$ represents the smoothed evaluation of the function $f_h(\boldsymbol{x})$, defined within the domain Ω, and is evaluated at a generic point $\mathbf{x} \in \Omega$. $W(|\boldsymbol{x}_i - \boldsymbol{x}_j|, h)$ denotes the interpolation or smoothing kernel function, and h stands for the smoothing length, which establishes the boundary for interactions with nearby particles. Applying the mean value theorem, we ensure that $\mathrm{x}_j \in$ Î©$_\mathrm{j}$ for every neighbouring particle j of the observation particle, *i.* Eq. (1) can be modified as indicated in Eq. (2) (Bonet and Kulasegaram, 2000), where V_j represents the volume of Î©$_\mathrm{j}$. In SPH practical applications, it is common to substitute the particle volume, represented as V_j, with the ratio of the mass of the particle j (m_j) to the density of particle j (ρ_j) in Eq. (3). By following analogous procedures, the particle representation of Eq. (3) can be expressed in terms of the gradient of the function, $f_h(\boldsymbol{x})$ from Eq. 4.

$$f_h(\boldsymbol{x}) \simeq \sum_{j=1}^{m} f(\boldsymbol{x}_j) W(|\boldsymbol{x}_i - \boldsymbol{x}_j|, h) V_j \tag{2}$$

$$f_h(\boldsymbol{x}) \simeq \sum_{j=1}^{m} \frac{m_j}{\rho_j} f(\boldsymbol{x}_j) W(|\boldsymbol{x}_i - \boldsymbol{x}_j|, h) \tag{3}$$

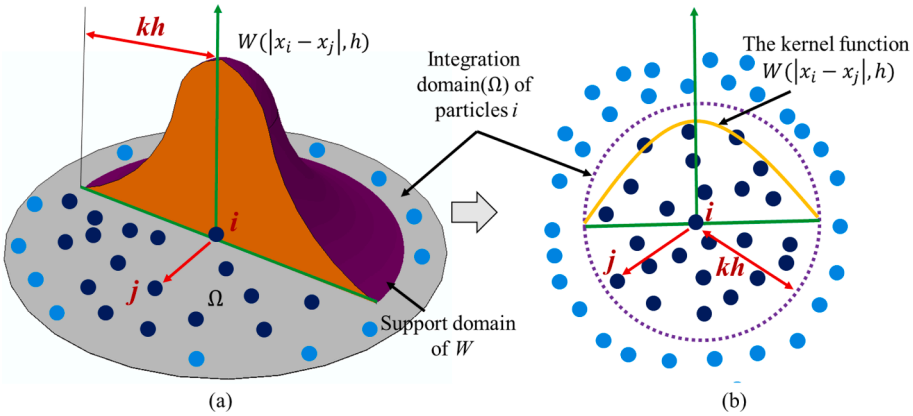

Fig. 1. The interaction of particles mediated by the kernel function in domain Ω **(a)** Representation of three-dimensional space **(b)** Representation in a plane.

$$\nabla f_h(\boldsymbol{x}) \simeq \sum_{j=1}^{m} \frac{m_j}{\rho_j} f(\boldsymbol{x}_j) \nabla W(|\boldsymbol{x}_i - \boldsymbol{x}_j|, h) \quad (4)$$

To finalise the discretisation, it is necessary to establish the kernel function considering factors such as the desired smoothness, accuracy, and computational efficiency. In general, $W(|\boldsymbol{x}_i - \boldsymbol{x}_j|, h)$ is a bell-shaped function characterised by specific criteria. It must satisfy the normalisation condition mentioned in Eq. (5) and converge to the Dirac delta distribution as $h \to 0$, be positive definite, exhibit even symmetry ($W(|\boldsymbol{x}_i - \boldsymbol{x}_j|, h) = W(|\boldsymbol{x}_j - \boldsymbol{x}_i|, h)$). The $\langle f_h(x) \rangle \to f_h(x)$ only when the set of consistency relations for the kernel's moments are fulfilled as stated in Eq. (6) (Sigalotti et al., 2021). The symbol l represents the rank of a matrix tensor, with values ranging from 1 and beyond, $0(l)$ represents the zero tensor of rank l.

$$\int W(|\boldsymbol{x}_i - \boldsymbol{x}_j|, h) d\Omega = 1 \quad (5)$$

$$M_l = \int (\boldsymbol{x}_i - \boldsymbol{x}_j)^l W(|\boldsymbol{x}_i - \boldsymbol{x}_j|, h) d\Omega = 0^l \quad (6)$$

Contemporary SPH applications typically use kernels with compact support, where $W(|\boldsymbol{x}_i - \boldsymbol{x}_j|, h)$ becomes zero outside the smoothing length. There are many options available, encompassing various kernel function types, from polynomial to Gaussian. One of the widely favoured functions is the quintic spline kernel, for which the definition for the 3-dimensional domain is as follows:

$$W(|\boldsymbol{x}_i - \boldsymbol{x}_j|, h) = \frac{7}{40\pi h^3} \begin{cases} \left(2 - \frac{|\boldsymbol{x}_i - \boldsymbol{x}_j|}{h}\right)^5 - 16\left(1 - \frac{|\boldsymbol{x}_i - \boldsymbol{x}_j|}{h}\right)^5 ; \frac{|\boldsymbol{x}_i - \boldsymbol{x}_j|}{h} \le 1 \\ \left(2 - \frac{|\boldsymbol{x}_i - \boldsymbol{x}_j|}{h}\right)^5 ; 1 < \frac{(|\boldsymbol{x}_i - \boldsymbol{x}_j|)}{h} \le 2 \\ 0; \quad \frac{|\boldsymbol{x}_i - \boldsymbol{x}_j|}{h} > 2 \end{cases} \quad (7)$$

In the Lagrangian approach, the conservation of mass is upheld through the continuity equation, while momentum conservation is expressed via the Euler equations, which track material particles. The Lagrangian approach describes the conservation equations for mass and momentum for the SPH particles as described in Eqs. (8) and (9):

$$\frac{D\rho}{Dt} = -\rho \nabla . \mathrm{v} \quad (8)$$

$$\frac{Dv}{Dt} = \frac{\nabla . \sigma}{\rho} = \nabla . \left(\frac{\sigma}{\rho}\right) + \frac{\sigma}{\rho^2} \nabla \rho \quad (9)$$

$$\sigma = S - p\delta_{ij} \quad (10)$$

In this context, ρ stands for mass density, σ represents the stress tensor, $\boldsymbol{v}$ denotes velocity and ∇ indicates the gradient operator. The stress tensor (σ) can be decomposed into hydrostatic stress $(-p\delta_{ij})$ governed by volume changes and deviatoric components (S) influence shape change in Eq. (10). In the SPH method, a contact model is used to simulate interactions between solid particles. When the particles representing the tool and workpiece intersect, they establish an interface, by the tool-workpiece particle contact model. The contact region exhibits a semi-elliptical pressure distribution, while the interface between these two particles assumes a circular shape, with the highest pressure concentration occurring at its centre. The Hertz contact model defines the magnitude of the interaction force (F) between the SPH particles representing the tool and workpiece as in Eq. (11) (Sharma et al., 2023; Lai et al., 2021).

$$F = \frac{4}{3} E_{eq} {R_{eq}}^{0.5} d^{1.5} \quad (11)$$

$$\frac{1}{E_{eq}} = \frac{1 - {\nu_t}^2}{E_t} + \frac{1 - {\nu_w}^2}{E_w} \quad (12)$$

$$\frac{1}{R_{eq}} = \frac{1}{R_t} + \frac{1}{R_w} \quad (13)$$

In these equations, E_{eq} represents the equivalent modulus (Eq. (12), where E_t and E_w stand for the elastic modulus of the tool and workpiece, respectively. Correspondingly, ν_t and ν_w denote the Poisson's ratios of the tool and workpiece. The variable d signifies the penetration depth. Additionally, R_{eq} signifies the equivalent radius of two smooth particles that are interacting, with radius R_t and R_w in Eq. (13). The developed SPH model considered the interaction between neighbouring particles, accounting for dynamic changes in stress and strain distributions with the Johnson-Cook flow stress model that characterises how a material plastically deforms (Yadav et al., 2023) and responds to external forces.

$$\sigma_{jc} = (A + B\varepsilon^{n_0}) \left[1 + C.ln\left(\frac{\dot{\varepsilon}}{\dot{\varepsilon}_0}\right)\right] \left[1 - \left(\frac{T - T_{ref}}{T_m - T_{ref}}\right)^m\right] \quad (14)$$

In this context, the terms ε and $\dot{\varepsilon}$ represent strain and strain rate, while A, B, C, n_0, and m are model constants that can be determined through a Split Hopkinson bar test (Jang et al., 2023). T and T_m respectively denote the instantaneous temperature generated during the cutting and melting temperature of the workpiece material. The algorithm adopted for the SPH simulation in the in-house code is illustrated in Fig. 2. In the nano-cutting process implemented on AFM instruments, heat generated from plastic deformation and friction is typically not a major concern due to marginal temperature rise resulting from relatively slow processing speeds. Therefore, the proposed process is modelled without accounting

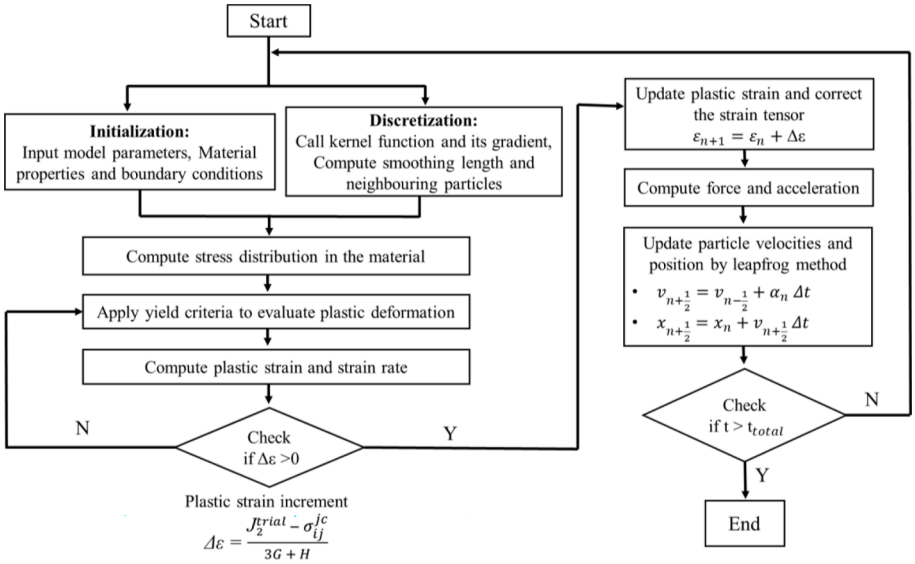

Fig. 2. Flowchart outlining the computation of SPH algorithm for nano-scratching simulation.

for thermal effects.

Table 1 displays the constants of the Johnson-Cook model, the mechanical properties of OFHC-Cu, and the cutting parameters used for nano-scratching.

2.2. Finite element method

A 3D finite element analysis was also conducted using the ABAQUS/Explicit v6.21 software. The analysis included an element deletion criterion that was triggered when a predefined fracture criterion was met, leading to the removal of the element without introducing excessive distortion errors. The material separation criterion employed a shear damage model, characterised by its stiffness degradation at a damage initiation and was controlled by fracture strain, strain rate, and shear stress ratio (Yadav et al., 2022). A damage initiation variable (ω) was defined as the ratio of increment in plastic failure strain ($d\varepsilon_f^p$) to failure strain at the onset of damage (ε_o^p) in Eq (15). A shear stress ratio (Eq. (16) was governed by the Von-Mises stress (σ_{eq}^v), pressure stress (σ_p) and maximum shear stress (τ_{max}).

$$\omega = \int \frac{d\varepsilon_f^p}{\varepsilon_0^p\left(\Theta, \varepsilon_f^p, \dot{\varepsilon}_f\right)} = 1 \tag{15}$$

$$\Theta = \frac{\sigma_{eq}^v + k\sigma_p}{\tau_{max}} \tag{16}$$

Table 1
Constants of the Johnson-Cook model, mechanical characteristics of OFHC-Cu, and the cutting parameters employed in the current investigation.

Johnson-Cook parameters (Zhang et al., 2020)				**Mechanical properties**		
A(MPa)	B(MPa)	C	n_0	Density (kg/m^3)	Elastic modulus (GPa)	Poisson's ratio (υ)
90	292	0.025	0.31	8930	117 GPa	0.34

Cutting parameters

Scratching depth (d): 20, 50, 100 and 150 nm
Negative rake angle (γ): 15°, 30° and 60°
Tip radius (r_e): 20, 50 and 100 nm

The sliding friction model was applied to the interaction between the AFM tip and workpiece featuring a friction coefficient of 0.15 (Wang et al., 2020). To enhance solution convergence and reduce the computational costs, a dynamic explicit time increment scheme was adopted. At each node, the weak form of the mechanical equilibrium equations was discretised addressed in Eq. (15), wherein [M] denotes the nodal mass matrix, $\{f_{int}\}$ and $\{f_{ext}\}$ denote the internal and externally applied forces respectively. The variable x and $\{\ddot{x}\}$, signifies the displacement and nodal acceleration at the time t_x.

$$[\mathrm{M}]\{\ddot{x}\} + f_{int}\{x\} = f_{ext}(t_x) \tag{17}$$

With the help of central difference rules, the velocity and the acceleration were approximated (Eqs. (18) and (19).

$$\dot{x}_{i+1/2} = \dot{x}_{i-1/2} + \frac{\Delta t_i + \Delta t_{i+1}}{2}\ddot{x} \tag{18}$$

$$x_{i+1} = u_i + \Delta t_i \dot{x}_{i+1/2} \tag{19}$$

2.3. Model establishment

The SPH and FE models were developed taking into account the confined domain of the AFM tip, which features a conical shape with a height of 300 nm. The workpiece was considered to have dimensions of 3 μm × 3 μm × 0.9 μm and made of OFHC-Cu material. The meshed model of the AFM tip made of diamond material was created using ABAQUS, and the nodal coordinates of the elements were assigned as SPH particles, as illustrated in Fig. 3(a). The scratching model, consisting of a tool and a workpiece, was discretised using SPH particles, as illustrated in Fig. 3(b). The assembly view for the FE model is presented in Fig. 3(c). A partition zone was established that equalled the magnitude of the cutting depth in the workpiece, ensuring a finer mesh (element size: 1 – 5 nm) in the scratching zone.

3. Results and discussion

This section presents a comprehensive analysis of how the cutting depth, cutting tip radius, and rake angle specifically affect cutting forces, groove dimensions, and the depth of deformation in the context of nano-scratching. In the context of investigating the effect of tooltip wear, particular attention is paid to the influence of tip radius on the cutting mechanism through both SPH and FE simulations. Fig. 4 illustrates the

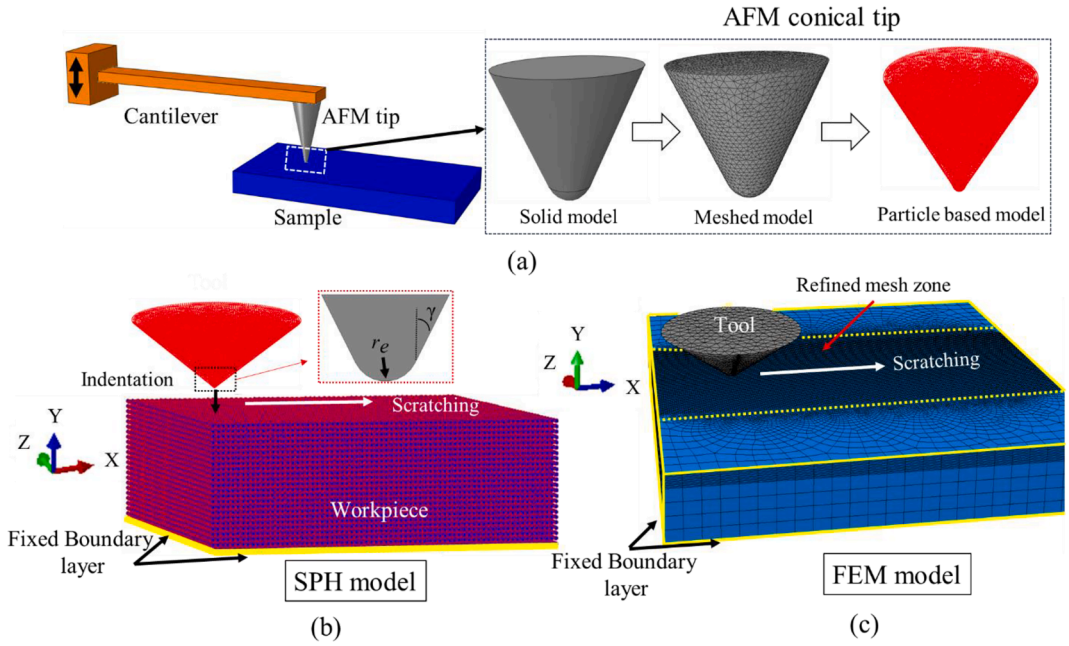

Fig. 3. **(a)** Discretisation of SPH particles for the AFM tip in the scratching model **(b)** Tool workpiece scratching model using SPH particles **(c)** The assembly mesh model of the tool and workpiece created with the FE tool Abaqus.

groove created with SPH simulation, considering various cutting depths for a tip radius of 100 nm.

The contour plot depicting the particle displacement of the scratched groove is shown in Fig. 4(a, c, e). The red colour indicates the significant displacement of workpiece particles pushed by the tool, particularly at the edge of the groove. The cross-section (x-x) of the groove is presented alongside a contour plot of the von Mises strain. An increase in cutting depth from 50 nm to 150 nm is shown in Fig. 4(b, d, f), the accumulation of more plastic strain near the scratched surface was observed due to intense plastic deformation experienced by the SPH particles. The comparison between the scratched groove simulated by SPH and FE modelling for 100 nm depth and 100 nm tip radius is shown in Fig. 5. In the nano-scratching setup, the tip was initially indented into the workpiece to the specified depth of cut. Subsequently, the tip moved parallel to the surface, removing material at the designated depth. The tip was retracted from the surface at the end, resulting in a nano-scale machined surface. The areas of indentation and scratching are depicted in Fig. 5(a, c), representing the distribution of von Mises plastic strain across the machined groove. In the SPH simulation, the maximum plastic strain reached a magnitude of 2, whereas in the FE simulation, it was 2.4. This discrepancy may be attributed to the damage model employed for material separation in FE, whereas the SPH model does not include a

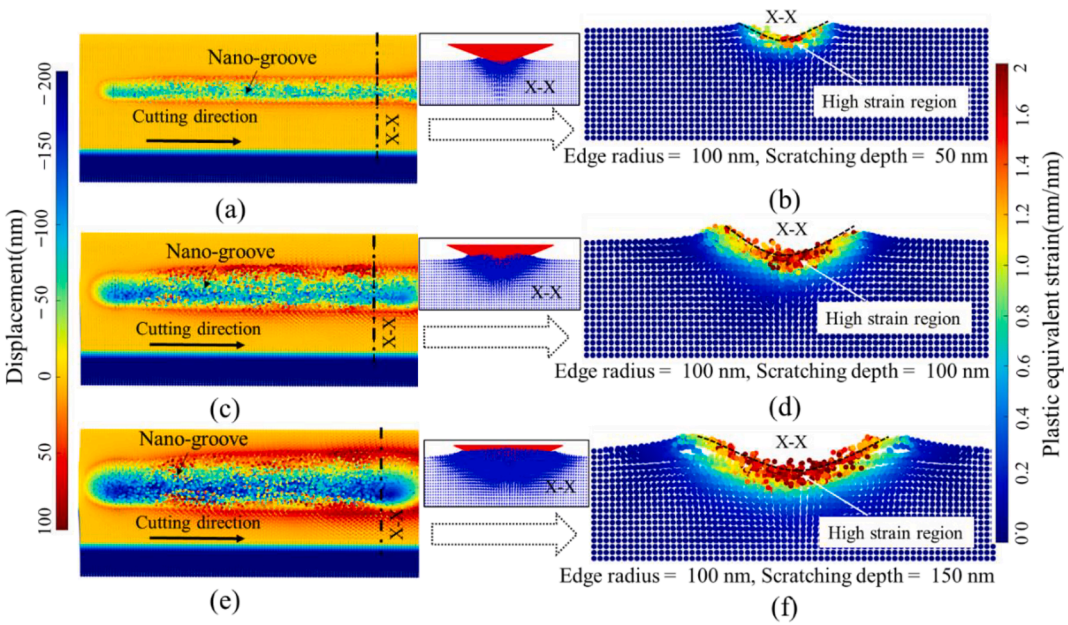

Fig. 4. Illustration of a scratched groove by SPH simulation showing displacement and von Mises strain for varying depths of scratching **(a, b)** 50 nm **(c, d)** 100 nm **(e, f)** 150 nm with the $r_e = 100$ nm and $\gamma = 60°$.

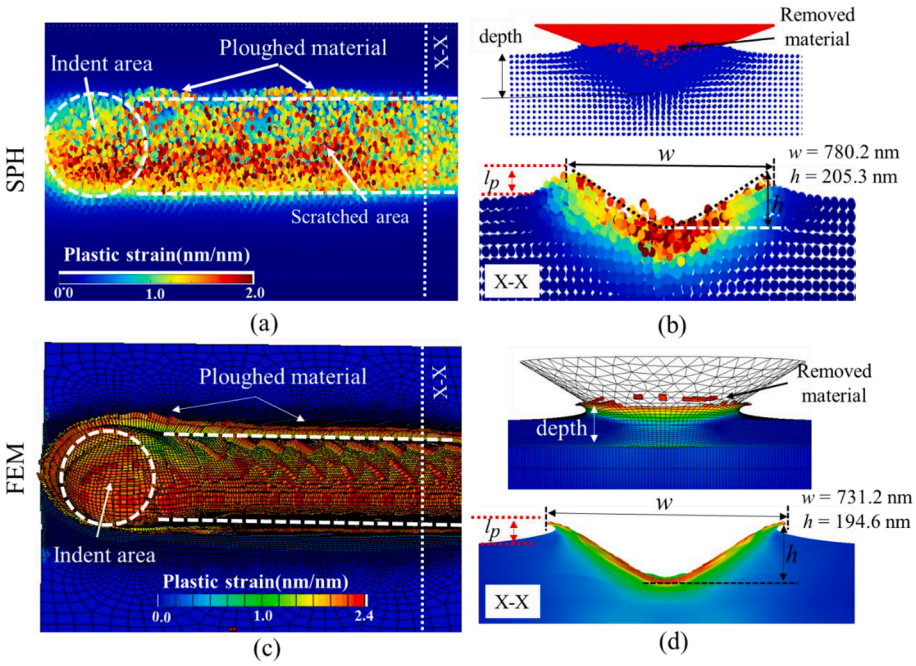

Fig. 5. A comparison of nano-scratched grooves **(a, b)** SPH simulation depicting von Mises contour and sectional view of groove showing the ploughed pile-up height l_p **(c, d)** FE simulation depicting von Mises contour and sectional view of groove showing l_p for 100 nm depth, r_e = 100 nm and $\gamma = 60°$.

damage criterion for particle separation.

While scratching, the material in front of the tooltip is pushed toward the top surface of the nano-groove due to the induced high contact pressure surpassing the shear flow strength of the material. Some material remains at the edge of the groove in the shape of pile-ups, a phenomenon referred to as ploughing. The sectional view of the machined groove is displayed in Fig. 5(b, d) along with the estimated width and height. It is noteworthy that the vertical dimension of the groove exceeds the designated cutting depth of 100 nm. This is attributed to the ploughing of material, contributing to the additional height, denoted as l_p. In the FE simulation, element deletion was employed and such a process was initiated when the damage value reached 0.95. As shown in Fig. 5, the FE simulation projected a groove width and a vertical dimension (w = 731.2 nm, h = 194.6 nm) lower than that of the SPH simulation (w = 780.2 nm, h = 205.3 nm) due to the elimination of elements during material separation and ploughing.

A parallel comparison was conducted for scratched grooves at various depths of 20 nm, 50 nm, 100 nm, and 150 nm using SPH and FE simulations as shown in Fig. 6. The groove width calculated through SPH simulation is consistently 5.89 to 6.92 % higher compared to that obtained with the FE method. Fig. 7 presents the average values of groove width and vertical dimension for different values of cutting tip radius, cutting depth, and rake angle. These average data were systematically obtained from ten different locations as illustrated in Fig. 7

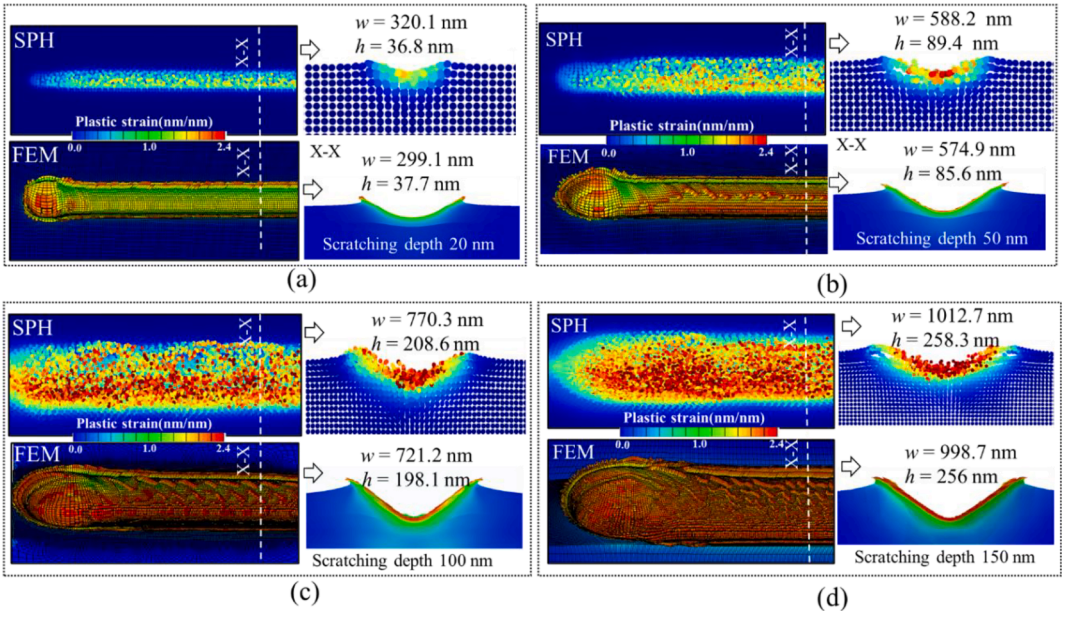

Fig. 6. A comparison of nano-scratched grooves dimensions between SPH and FE simulation for different scratching depths **(a)** 20 nm **(b)** 50 nm **(c)** 100 nm and **(d)** 150 nm for 100 nm depth and r_e = 100 nm and $\gamma = 60°$.

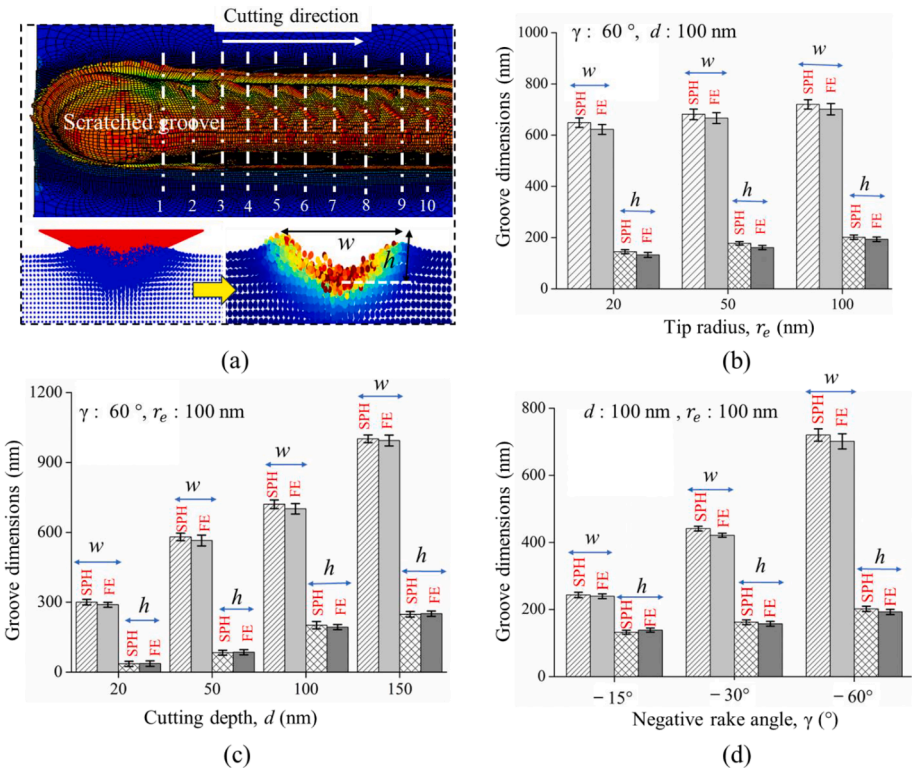

Fig. 7. **(a)** Illustrating the positions where width and height measurements were taken on the scratched groove; dependency of groove dimensions on **(b)** Tip radius, **(c)** Cutting depth, and **(d)** Rake angle.

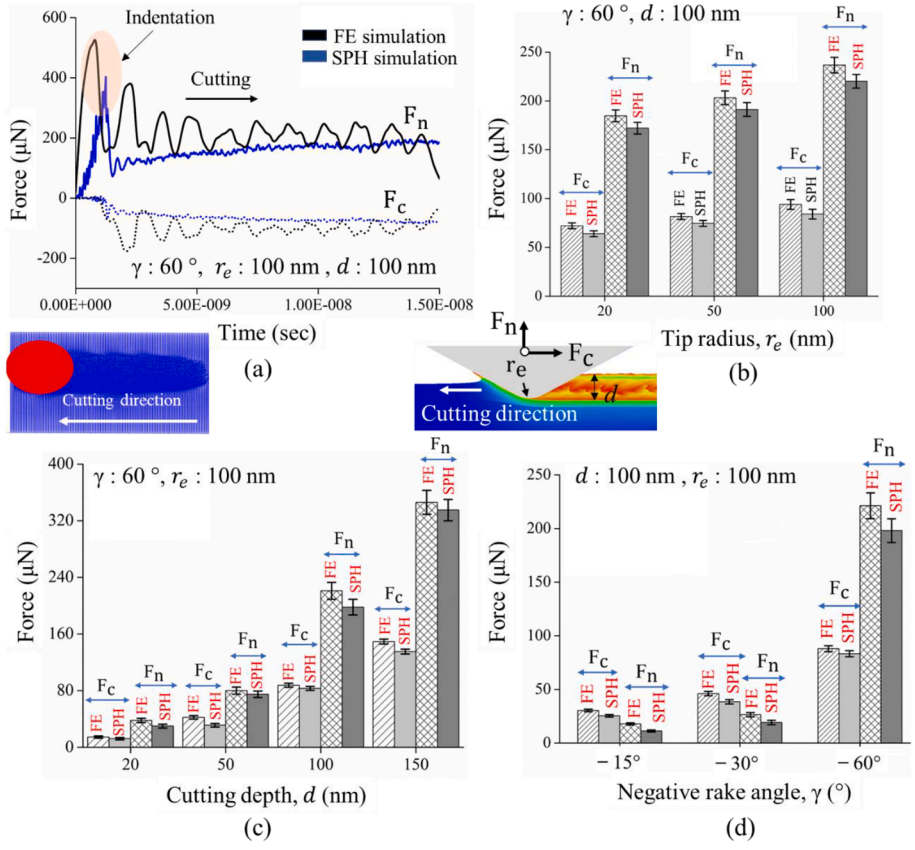

Fig. 8. **(a)** Comparison of the force trends between SPH and FE models **(b)** Forces variation with tip radius **(c)** Forces variation with cutting depth **(d)** Forces variation with rake angle of the tool ($\mathbf{F_n}$ – normal force, $\mathbf{F_c}$ – cutting force).

(a). The dimensions of the groove, both width and vertical dimensions, increased as the tip radius increased from 20 nm to 100 nm, as shown in Fig. 7(b).

A larger tip radius results in a wider scratched groove due to the conical shape of the AFM tip. Furthermore, as the tip radius increased, material separation occurred in the proximity of the cutting-tip radius, causing the material to flow along the tip radius rather than the rake surface. This led to a local negative rake angle, contributing to increased ploughing and consequently, a higher groove vertical height. An increased cutting depth and a negative rake angle led to a larger groove width, primarily because of the wider engagement of the conical tool with the workpiece (Fig. 7(c)). The higher negative rake angle also led to the higher groove height due to more pronounced ploughing (Fig. 7(d)). Based on Fig. 7, it appears that the groove dimensions are almost the same with marginal deviations in both the SPH and FE calculations.

The comparison of cutting forces between SPH and FE simulations is depicted in Fig. 8(a). The SPH model exhibited a smoother variation in forces compared to the FE model. The fluctuation in cutting force in the FE model was caused by the element deletion criteria and severe distortion of mesh elements during plastic deformation. Therefore, the study reveals one of the advantages of considering the meshless SPH model. Initially, the normal force increases due to the tip's indentation into the workpiece and then drops after the scratching commences. During initial indentation, the tool contacts neighbouring particles in radial directions. As scratching begins, the tool loses contact with the particles not intersecting the tip path, reducing the normal force. As shown in Fig. 8(a), the normal forces were observed to exceed the cutting forces for a specified depth of cut of 100 nm with a highly negative rake angle of 60°. This phenomenon is attributed to the influence of the negative rake angle. A substantial normal force leads to significant ploughing, involving the plastic deformation of the material, which becomes a crucial mechanism for generating nano-scale grooves. For a given cutting depth, the forces were higher for a larger tip radius, as illustrated in Fig. 8(b), owing to tool bluntness and larger contact area. Increased cutting depth resulted in larger forces, primarily because of the greater engagement of uncut material with the tool, as depicted in Fig. 8(c). Zhu et al., (2010) also observed analogous phenomena through MD simulations. This figure also shows that for the 100 nm tip radius and $\gamma = 60°$, normal forces are always higher than the cutting forces. Further, Fig. 8(d) reveals that an increase in negative rake angle (γ) from 15° to 30° resulted in forces increasing relatively slowly, in comparison, with a further increase in the γ to 60°. The normal force exhibits a non-linear behaviour that leads to an exponential increase. This phenomenon suggests that at a $\gamma = 60°$, there is a potential shift in the mechanism, leading to dominance by ploughing.

The robustness of the proposed model was verified in terms of the cutting and normal force with the reported experimental results proposed by Islam et al., 2012 with the same cutting parameters. Fig. 9(a, b) illustrates the force variations for a scratching depth of 100 nm, while Fig. 9(c, d) depict the results for a scratching depth of 150 nm. The forces were assessed at the initiation of the scratching process following the tool indentation. The simulated forces exhibited a trend consistent with the experimental results, with magnitudes deviating by 13 % for 100 nm scratching depth (Fig. 9(a, b, c)).

This slight force discrepancy could be attributed to the rigid constraint applied to the tool in the present simulation. Additionally, in real experiments, the deflection of the cantilever beam used in AFM can impact both the scratching depth and the orientation of the tip, potentially introducing inaccuracies. Moreover, at a scratching depth of 150 nm, there was an 18 % deviation in the cutting force magnitude in the SPH simulation, illustrated in Fig. 9(d). This discrepancy could be attributed to instability caused by the applied Hertz contact model between particles. In the cutting process, high contact stresses at the tool-workpiece interface induce and surpass the shear flow strength of the work material (Childs, 2006). Consequently, the stick–slip phenomenon becomes pivotal, necessitating a more effective friction algorithm. This

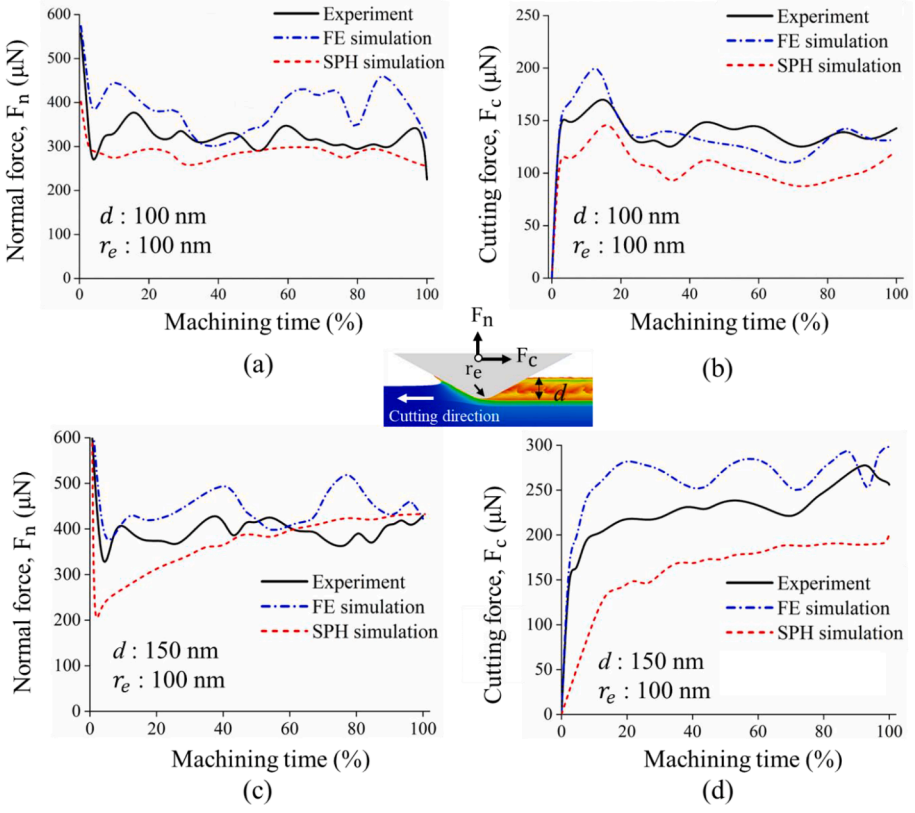

Fig. 9. Validation of normal and cutting forces with experimental results of (Islam et al., 2012) for (a, b) Normal and cutting force at 100 nm depth (c, d) Normal and cutting force at 150 nm depth with $r_e = 100$ nm and $\gamma = 60°$.

phenomenon underscores a potential limitation of the SPH algorithm used in these machining simulations.

As tip wear progresses, the geometry changes, affecting the ability of the tool to shear material effectively. Increased tip wear may shift the mechanism from cutting to ploughing, leading to higher ploughing forces. Understanding the effects of tip wear is critical for maintaining machining precision and achieving desired outcomes in nano-scale material removal processes. In the current study, the scalar ratio of the scratching depth (d) and tip radius (r_e) is chosen to analyse the cutting mechanism. Fig. 10(a) shows the variation of force ratio (F_n/F_c) with the scalar ratio d/r_e. As wear advances, the tip radius increases, leading to a decrease in the d/r_e ratio for a constant scratching depth. For the case of $\gamma = 15^\circ$ rake angle, the force ratio increased with a decrease in d/r_e from 2 to 0.42, commencing the ploughing effect, despite the cutting force being greater than the normal force within this range. With a further reduction in the d/r_e ratio from 0.42, the force ratio exponentially increased in this range due to the dominance of the normal force over the cutting force, driven by ploughing. At a $\gamma = 60^\circ$ rake angle, the force ratio consistently remains above 1, indicating that the normal force is higher than the cutting force due to the dominant effect of ploughing over cutting.

A transition occurs when the d/r_e ratio equals or falls below 0.3, i.e. when the scratching depth is 30 % of tip radius, resulting in a transformation from cutting to ploughing. The material exhibited side flow only at the vicinity of the tip radius rather than being cut under high contact pressure shown in Fig. 10(c). It is well known that the critical ratio of d/r_e, at which the transition from cutting to ploughing occurs, depends on both the tool tip radius and material properties (Malekian et al., 2012). De Oliveira et al., (2015) measured a critical ratio range of 0.25 to 0.33 for OFHC-Cu and the results simulated here fall within this specified range. The critical tip radius for altering forces was observed to be 238 nm at a scratching depth of 100 nm and 15° negative rake angle indicated by the force variation in Fig. 10(b).

Nano-machining induces residual strain, a crucial factor in material behaviour at the nanoscale, that impacts the surface integrity. Investigating residual strain in nano-machining is essential for enhancing the performance and reliability of nano-components. Sectional views of nano-grooves with von Mises strain contour for SPH and FE simulation are reported in Fig. 11(a, b). The layer near the machined surface deformed severely due to direct contact with the tool, therefore the plastic strain magnitude is maximum. The influence of plastic deformation diminishes with increasing distance from the top surface of a machined surface, correlating with the reduction in cutting force intensity deeper into the material (Kermouche et al., 2010).

Fig. 11(c, d) illustrates the plastic deformation in the cross-section for different scratching depths and tip radii. The average deformation thickness was simulated with SPH and FEM. With an increase in the scratching depth, the thickness of the deformed layer increased due to the induction of higher cutting forces. The maximum deformation depth was $3.6r_e$, observed for 150 nm scratching depth (Fig. 12(a)). In nanoscale machining, using a higher tip radius results in a deeper deformation. This is attributed to the increased contact area, concentrating forces over a larger volume.

Fig. 12(b) shows that the maximum deformed thickness was $2.3r_e$, for 100 nm scratching depth with 60° negative rake. In Fig. 12(c), the deformed layer thicknesses resulting from nanoscale surface scratching $\gamma = 15^\circ$, 30°, and 60°, rake angle tools are presented. Higher negative rake angles typically result in higher cutting forces. These increased forces contribute to a more significant plastic deformation of the material, leading to a thicker deformed layer. The bar chart in Fig. 12(c) illustrates that the deformed thickness increased by 58 % with an increase in γ from 15° to 60°. Dai et al., (2019b) made comparable

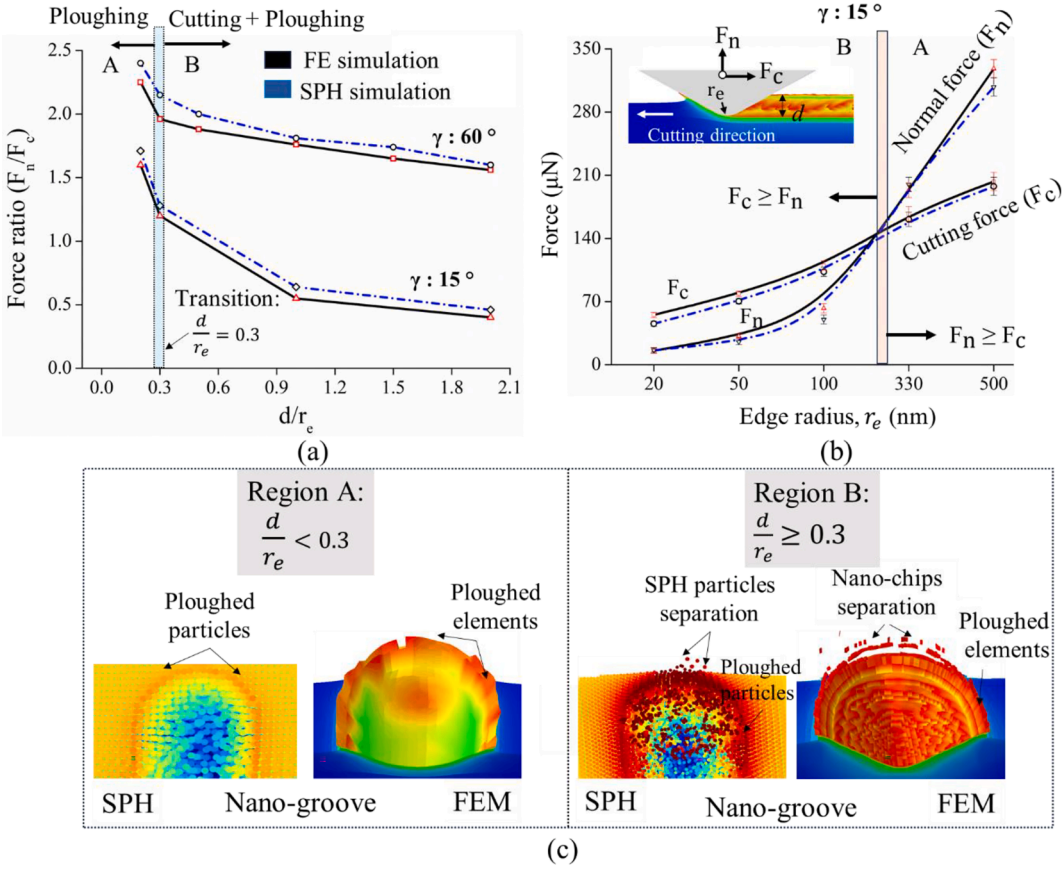

Fig. 10. **(a)** Variation of force ratio with d/r_e for different rake angles **(b)** Variation of normal and cutting forces with tip radius for 100 nm depth and $\gamma = 15^\circ$ **(c)** The nano-groove at the end of cut in different regimes obtained through SPH and FEM simulations.

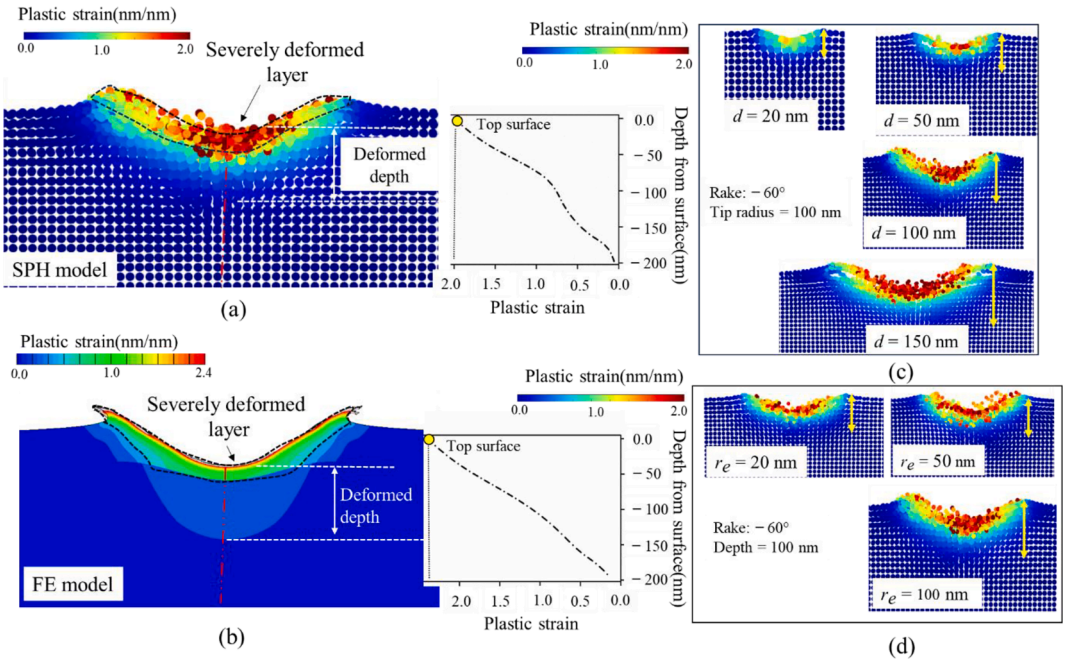

Fig. 11. Illustrating deformed layer with von Mises plastic strain distribution **(a)** SPH simulation **(b)** FEM simulation **(c)** Sectional view of nano-scratched groove for different scratching depth with tip radius of 100 nm **(d)** Sectional view of nano-scratched groove for different tip radii with scratching depth of 100 nm and $\gamma = 60°$.

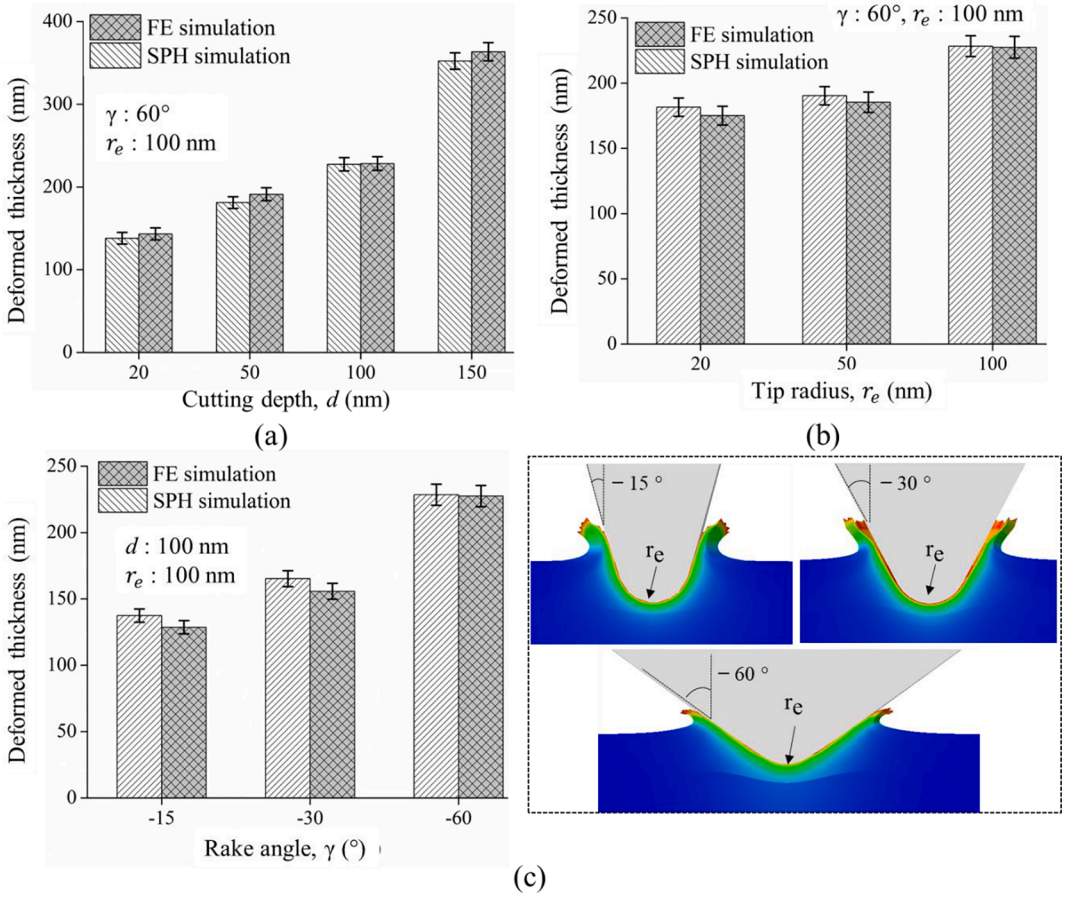

Fig. 12. Simulated deformed thickness of nano-groove with different **(a)** Cutting depths **(b)** Tip radii and, **(c)** Rake angles.

observations regarding surface deformation and forces, which were influenced by tip radius and rake angle in simulations conducted through the molecular dynamics approach.

4. Conclusions

This study proposed and compared the mesh-free SPH and the FEM techniques to model nanoscale scratching on OFHC-Cu with tools featuring a negative rake angle. It investigated the influence of scratching depths, negative rake angles, and tooltip radius on contact forces, surface topography, and deformed layer thickness. For practitioners, the study showed the importance of deploying an effective tip monitoring procedure when implementing the AFM-based nano-scratching process. In particular, tip wear was shown to lead to a transition from a cutting-dominated to a ploughing-dominated regime, with associated variations in resulting groove geometry and plastic strain, when the tip radius reached 30 % of the scratching depth of the OFHC-Cu work material. The simulation results were also validated with experimental data from the literature, leading to the following conclusions:

- A larger tip radius of the tool widens the scratched groove owing to its conical shape. Material separation in the vicinity of the tip radius results in a local negative rake angle, leading to ploughing. This increased groove height. The higher cutting depth and negative rake angle produce a wider groove due to the wider engagement of the conical tool with the workpiece.
- A higher tip radius led to higher cutting forces due to tool bluntness and an increased contact area. Higher cutting depths contributed to the higher forces primarily driven by the larger volume of material engaged with the tool. The sensitivity of normal forces was observed to be higher with a $\gamma = 60^\circ$ rake angle, attributed to the dominance of the ploughing mechanism over cutting. For the 15° and 30° negative rake angle tools, the ploughing mechanism was slightly more predominant at lower scratching depths and higher tip radius.
- Cutting forces exceeded normal forces for $\gamma = 15^\circ$, until the scratching depth reached 42 % of the tip radius. Below this depth, a shift in force dynamics occurred, with normal forces predominating due to the prominence of ploughing. The transition from cutting to ploughing was observed at a scratching depth of 30 % of the tip radius for OFHC-Cu, regardless of the rake angle, indicating lateral material flow under intense contact pressure.
- The effect of plastic deformation lessens with increasing distance from the top surface of a nano-groove, owing to a decrease in cutting force intensity deeper into the material. The top surface exhibited a maximum von Mises plastic strain value more than 2.0 in both FE and SPH simulations. As the scratching depth and tip radius increased, the thickness of the deformed layer also increased due to the induction of higher normal and cutting forces. The maximum deformation depth, observed at a scratching depth of 150 nm with a $\gamma = 60^\circ$ negative rake angle, reached 3.6 times the tip radius. Additionally, the deformed thickness increased by 58 % with γ changing from 15° to 60°.
- The FEM model exhibited higher fluctuations in cutting forces as a result of damage and element deletion criteria during severe distortion of the elements. Therefore, the SPH model proves advantageous in such circumstances. Additionally, at greater scratching depths, the SPH model showed greater inaccuracies due to the intense contact stress induced at the chip-tool interface. Therefore, the FEM model is advantageous in this respect.

The present investigation employed SPH and FEM modelling approaches to simulate nanoscale scratching of OFHC-Cu material. To improve the proposed modelling methods, the following modifications can be considered for future scope:

- In nano-scale machining, the strain gradient effect becomes pronounced as material properties exhibit sensitivity to localised deformation. At this scale, flow stress is influenced not only by plastic strain but also by the strain gradient, significantly affecting material response, surface integrity, and deformation characteristics. Integrating strain gradient considerations could enhance the current SPH and FEM modelling methodologies in nanoscale scratching studies.
- The cantilever beam deflection in AFM-based nano-cutting can compromise accuracy by altering the AFM tip position and inducing dynamic instability. This deflection leads to variations in applied forces, tool wear, and material deformation, affecting the precision of cuts and surface finish. Therefore, the current investigation could be improved by considering the influence of cantilever deflection on nano-scale cutting.

CRediT authorship contribution statement

Rahul Yadav: Writing – original draft, Validation, Investigation, Data curation. **Anuj Sharma:** Software. **Sivakumar Kulasegaram:** Writing – review & editing, Supervision, Methodology, Funding acquisition. **Sahar Alimohammadi:** Writing – review & editing. **Dan Read:** Writing – review & editing, Supervision, Funding acquisition. **Emmanuel Brousseau:** Writing – review & editing, Supervision, Project administration, Funding acquisition.

Declaration of competing interest

The authors declare that they have no known competing financial interests or personal relationships that could have appeared to influence the work reported in this paper.

Data availability

Data will be made available on request.

Acknowledgments

The reported research was funded by the Engineering and Physical Sciences Research Council (EPSRC) under the grant EP/T01489X/1. We would like to thank Supercomputing Wales for allowing us to run our code efficiently in the HAWK supercomputing system. All data created during this research are openly available from Cardiff University data archive at http://doi.org/10.17035/d.2024.0315996761.

References

Bhushan, B., Israelachvili, J., Landman, U., 1995. Nanotribology: friction, wear and lubrication at the atomic scale. Nature 374, 607–616. https://doi.org/10.1038/374607a0.

Bonet, J., Kulasegaram, S., 2000. Correction and stabilization of smooth particle hydrodynamics methods with applications in metal forming simulations. Int. J. Numer. Methods Eng. 47, 1189–1214.

Chen, Y., Hu, Z., Jin, J., Li, L., Yu, Y., Peng, Q., Xu, X., 2021. Molecular dynamics simulations of scratching characteristics in vibration-assisted nano-scratch of single-crystal silicon. Appl. Surf. Sci. 551 (2021), 149451 https://doi.org/10.1016/j.apsusc.2021.149451.

Childs, T.H.C., 2006. Friction modelling in metal cutting. Wear 260 (3), 310–318. https://doi.org/10.1016/j.wear.2005.01.052.

Dai, H., Li, S., Chen, G., 2019a. Molecular dynamics simulation of subsurface damage mechanism during nanoscratching of single crystal silicon. Proc. Inst Mech. Eng. Part J J. Eng. Tribol. 233, 61–73. https://doi.org/10.1177/1350650118765351.

Dai, H., Du, H., Chen, J., Chen, G., 2019b. Investigation of tool geometry in nanoscale cutting single-crystal copper by molecular dynamics simulation. Proc. Inst Mech. Eng. Part J J. Eng. Tribol. 233, 1208–1220. https://doi.org/10.1177/1350650119826448.

De Oliveira, F., Rodrigues, A., Coelho, R., de Souza, A., 2015. Size effect and minimum chip thickness in micromilling. Int. J. Mach. Tools Manuf. 89, 39–54. https://doi.org/10.1016/j.ijmachtools.2014.11.001.

Gingold, R., Monaghan, J., 1977. Smoothed particle hydrodynamics: theory and application to non-spherical stars. Mon. Not. R. Astron. Soc. 181, 375–389. https://doi.org/10.1093/mnras/181.3.375.

Guo, Z., Tian, Y., Liu, X., Wang, F., Zhou, C., Zhang, D., 2017. Modeling and simulation of the probe tip based nanochannel scratching. Precis. Eng. 49, 136–145. https://doi.org/10.1016/j.precisioneng.2017.02.002.

Islam, S., Ibrahim, R., Das, R., Fagan, T., 2012. Novel approach for modelling of nanomachining using a mesh-less method. Appl. Math. Model. 36, 5589–5602. https://doi.org/10.1016/j.apm.2012.01.005.

Jang, T.J., Yoon, J.W., Kim, J.B., 2023. Determination of Johnson-Cook constitutive model coefficients considering initial gap between contact faces in SHPB test. J. Mater. Res. Technol. 24, 7242–7257. https://doi.org/10.1016/j.jmrt.2023.05.001.

Jian-Hao, C., Qiu-Yang, Z., Zhen-Yu, Z., Cong, D., Zhong-Yu, P., 2021. Molecular dynamics simulation of monocrystalline copper nano-scratch process under the excitation of ultrasonic vibration. Mater. Res. Express. 8, 46507. https://doi.org/10.1088/2053-1591/abf2eb.

Kawasegi, N., Takano, N., Oka, D., Morita, N., Yamada, S., Kanda, K., Takano, S., Obata, A., 2006. Nanomachining of silicon surface using atomic force microscope with diamond tip. J Manuf Sci Eng. 128 (3), 723–729. https://doi.org/10.1115/1.2163364.

Kermouche, G., Rech, J., Hamdi, H., Bergheau, J.M., 2010. On the residual stress field induced by a scratching round abrasive grain. Wear 269 (1–2), 86–92. https://doi.org/10.1016/j.wear.2010.03.012.

Kong, X., Deng, J., Dong, J., Cohen, P., 2020. Study of tip wear for AFM-based vibration-assisted nanomachining process. J. Manuf. Process. 50, 47–56. https://doi.org/10.1016/j.jmapro.2019.12.013.

Lai, Z., Chen, Q., Huang, L., 2021. A semianalytical Hertzian frictional contact model in 2D. Appl. Math. Model. 92, 546–564. https://doi.org/10.1016/j.apm.2020.11.016.

le Zhu, W., Yang, Y., Li, H.N., Axinte, D., Beaucamp, A., 2019. Theoretical and experimental investigation of material removal mechanism in compliant shape adaptive grinding process. Int. J. Mach. Tools Manuf. 142, 76–97. https://doi.org/10.1016/j.ijmachtools.2019.04.011.

Leroch, S., Varga, M., Eder, S.J., Vernes, A., Ripoll, M.R., Ganzenmüller, G., 2016. Smooth particle hydrodynamics simulation of damage induced by a spherical indenter scratching a viscoplastic material. Int. J. Solids Struct. 81, 188–202. https://doi.org/10.1016/j.ijsolstr.2015.11.025 0020-7683.

Lucy, L.B., 1977. A numerical approach to the testing of the fission hypothesis. Astron. J. 82, 1013–1024. https://doi.org/10.1086/112164.

Malekian, M., Mostofa, M.G., Park, S.S., Jun, M.B.G., 2012. Modeling of minimum uncut chip thickness in micro machining of aluminum. J. Mater. Process. Technol. 212 (3), 553–559. https://doi.org/10.1016/j.jmatprotec.2011.05.022.

Meng, B., Yuan, D., Xu, S., 2019. Study on strain rate and heat effect on the removal mechanism of SiC during nano-scratching process by molecular dynamics simulation. Int. J. Mech. Sci. 151, 724–732. https://doi.org/10.1016/j.ijmecsci.2018.12.022.

Mo, Y., Zhao, W., Zhu, M., Bai, M., 2008. Nano/microtribological properties of ultrathin functionalized imidazolium wear-resistant ionic liquid films on single crystal silicon. Tribol. Lett. 32, 143–151. https://doi.org/10.1007/s11249-008-9371-9.

Qi, Y., He, T., Xu, H., Hu, Y., Wang, M., Feng, M., 2021. Effects of microstructure and temperature on the mechanical properties of nanocrystalline CoCrFeMnNi high entropy alloy under nanoscratching using molecular dynamics simulation. J. Alloys Compd. 871, 159516 https://doi.org/10.1016/j.jallcom.2021.159516.

Sharma, A., Kulasegaram, S., Brousseau, E., Esien, K., Read, D., 2023. Investigation of nanoscale scratching on copper with conical tools using particle-based simulation. Nanomanufacturing and Metrology 6 (1). https://doi.org/10.1007/s41871-023-00179-5.

Sigalotti, L., Klapp, J., Gesteira, M., 2021. The mathematics of smoothed particle hydrodynamics (SPH) consistency. Front. Appl. Math. Stat. 7, 797455 https://doi.org/10.3389/fams.2021.797455.

Wang, W., Hua, D., Luo, D., Zhou, Q., Li, S., Shi, J., Wang, H., 2022. Molecular dynamics simulation of deformation mechanism of CoCrNi medium entropy alloy during nanoscratching. Comput. Mater. Sci. 203, 111085 https://doi.org/10.1016/j.commatsci.2021.111085.

Wang, Q., Yang, Y., Yao, P., Zhang, Z., Yu, S., Zhu, H., Huang, C., 2020. Friction and cutting characteristics of micro-textured diamond tools fabricated with femtosecond laser. Tribol. Int. 154, 106720 https://doi.org/10.1016/j.triboint.2020.106720.

Xie, H., Ma, Z., Zhao, H., Ren, L., 2022. Temperature induced nano-scratch responses of γ-TiAl alloys revealed via molecular dynamics simulation. Mater. Today Commun. 30, 103072 https://doi.org/10.1016/j.mtcomm.2021.103072.

Yadav, R., Chakladar, N.D., Paul, S., 2022. Micro-milling of Ti-6Al-4 V with controlled burr formation. Int. J. Mech. Sci. 231, 107582 https://doi.org/10.1016/j.ijmecsci.2022.107582.

Yadav, R., Chakladar, N.D., Paul, S., 2023. Efects of tailored residual stress on micro–end milling: numerical modelling and validation. Int. J. Adv. Manuf. Technol. 127, 5449–5470. https://doi.org/10.1016/j.jmapro.2022.03.040.

Yin, Z., Zhu, P., Li, B., 2021. Study of nanoscale wear of SiC/Al nanocomposites using molecular dynamics simulations. Tribol. Lett. 69, 1–17. https://doi.org/10.1007/s11249-021-01414-0.

Zhang, J., Xu, X., Outeiro, J., Liu, H., Zhao, W., 2020. Simulation of grain refinement induced by high-speed machining of OFHC copper using cellular automata method. J. Manuf. Sci. Eng. Trans. ASME. 142, 091006. https://doi.org/10.1115/1.4047431.

Zhang, P., Zhao, H., Shi, C., Zhang, L., Huang, H.R., 2013. Influence of double-tip scratch and single-tip scratch on nano-scratching process via molecular dynamics simulation. Appl. Surf. Sci. 280, 751–756. https://doi.org/10.1016/j.apsusc.2013.05.056.

Zhu, P., Hu, Y., Ma, T., Wang, H., 2010. Study of AFM-based nanometric cutting process using molecular dynamics. Appl. Surf. Sci. 256, 7160–7165. https://doi.org/10.1016/j.apsusc.2010.05.044.